International Journal of Non-Linear Mechanics 154 (2023) 104431

Contents lists available at ScienceDirect

International Journal of Non-Linear Mechanics

journal homepage: www.elsevier.com/locate/nlm

Snap-through instability during transmission of rotation by a flexible shaft with initial curvature

Yury Vetyukov [a,*], Evgenii Oborin [b]

[a] Institute of Mechanics and Mechatronics, TU Wien, Getreidemarkt 9, A-1060 Vienna, Austria
[b] Institute of Production Engineering and Photonic Technologies, TU Wien, Getreidemarkt 9, A-1060 Vienna, Austria

ARTICLE INFO

Keywords:
Kirchhoff rods
Snap-through instability
Geometric nonlinearity
Incremental deformations
Finite element analysis

ABSTRACT

The geometric imperfection of a flexible shaft transmitting rotary motion along a curved path may result in a highly nonlinear relation between the rotation angles at the driving and driven ends. If the intrinsic curvature of the shaft surpasses a specific threshold, even snap-through instability becomes possible. Previously, the problem has been considered for the case when the shaft is confined in a rigid channel such that only the rotary motion is possible along its entire length. The present study focuses on the case of the freely deformable axis of the shaft. Just the locations and the tangential directions of its ends are fixed. We investigate the response of the shaft, in terms of rotation at the driven end, by combining analytical solutions using incremental equations from the theory of Kirchhoff rods and a finite element model that features a C^1 continuous approximation of deflections and rotations. Comparison to the constrained case shows that the impact of the deformability of the axis grows both with the intrinsic curvature of the shaft and its angular length.

1. Introduction

Delivering rotary motion, torque and power from a motor to a distant point in space is essential for various applications like drilling, screw driving, robotics, etc. There are circumstances when a flexible shaft needs to be used for that purpose. Just to name a few: there may be obstacles between the motor and the point of action, the direction of rotary motion may need to be easily changeable or the point of action may be moving relative to the motor. For certain applications, vibration or thermal isolation between the motor and the tool is also important.[1] If a flexible shaft is rotating within a borehole or stiff housing (sleeve) in such a way that its axis takes on a shape dictated by the channel, then its particles may only undergo rotary motion. It is however known that a geometric imperfection of the shaft in the form of initial curvature (also known as natural, intrinsic, own, eigen- or pre-curvature) along with the curvature of the constraining channel may result in highly irregular rotation of the tool even at slow motion and in the absence of friction. In other words, the rotation angle at the exit (driven end) θ_{exit} can become a nonlinear or even not a single-valued function of the rotation angle at the entry (driving end) θ_{entry}, which has been studied in several publications both analytically and numerically [1–4]. Recently, the effect has also been studied in application to concentric tube robots, where the curvatures of the inner rod and the outer tube result in unstable "snapping" motions during the rotation of the inner rod [5]. Interestingly, the snap-through phenomenon, along with the release of elastic energy in a rapid dynamic process, has significant implications for a wide range of biophysical and applied physical problems, which deserves increasing attention of researchers both from the analytical as well as from the experimental perspectives; see papers [6–8] on in-plane buckling and [9] on the out-of-plane twist-bend instability of an elastic strip with prescribed rotation at the ends.

The present contribution focuses on a novel formulation of the problem: we consider the flexible shaft to be clamped at both ends, but free to deform in between. Its initial curvature will cause additional bending of the axis during rotation, which can alter the relation between θ_{entry} and θ_{exit} as compared to the constrained case. For simplicity, we do not take torque loading at the exit end into account and restrict our consideration to simple geometries of the mechanical system, which, however, provides us with insights regarding the differences between the behavior of constrained and freely deformable shafts.

The elastic response of a flexible shaft is reasonable to describe with a nonlinear 1D model of a rod. A classical Kirchhoff model with constrained shear shall be appropriate, because torsional and bending deformations are expected to play the dominant role. The literature provides various examples of geometrically nonlinear structural analysis using elastic rod models. These include analytical and experimental buckling analysis of a flexible elastica bending in a plane [6–8,10] or in 3D space with bending and twist [9,11,12], optimization with respect to resistance to buckling [13] or numerical approach based

* Corresponding author.
E-mail address: yury.vetyukov@tuwien.ac.at (Y. Vetyukov).

[1] See e.g. https://www.elliottmfg.com/2022/01/19/flexible-shafts-in-action/ for technical applications of the flexible transmission technology.

https://doi.org/10.1016/j.ijnonlinmec.2023.104431
Received 10 January 2023; Received in revised form 21 April 2023; Accepted 1 May 2023
Available online 9 May 2023

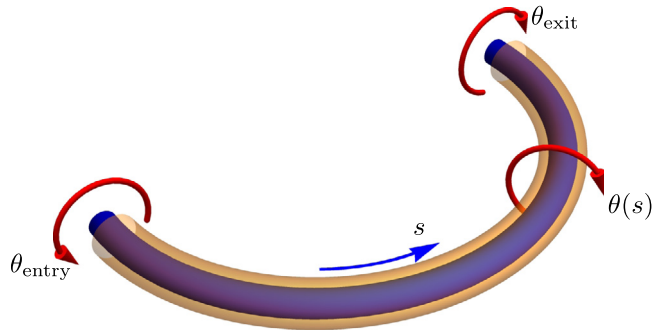

Fig. 1. Transmission of rotation by a flexible shaft in a rigid channel.

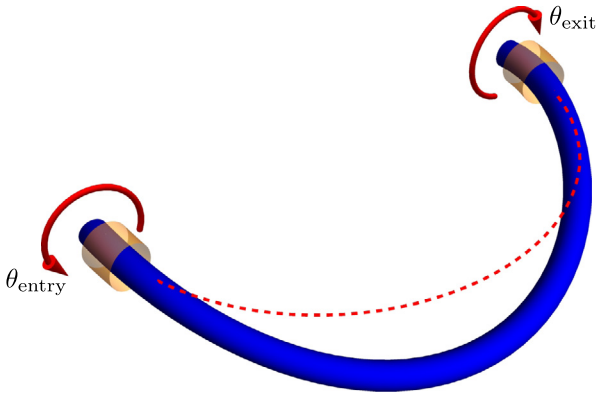

Fig. 2. Transmission of rotation by a freely deformable flexible shaft; initial curvature $\kappa \neq 0$ results in additional bending deformations in contrast to the ideal shape depicted by the dashed line.

on the parametrization of strains, allowing for the reconstruction of actual geometry through integration [14]. While the relations of the general nonlinear theory of rods are known since decades [15], the analytical part of the present investigation makes use of the incremental equations, linearized in the vicinity of a deformed state. For this purpose, we use the form of equations proposed by Eliseev [16], see also [17] for the presentation in English. The geometric imperfection of the rod, namely, its small initial curvature, is considered a perturbation parameter, thus extending the known equations by additional terms—similar to study [18]. We present a brief overview of the nonlinear and incremental equations in Appendix.

We numerically extend the closed form solution to arbitrarily large values of the intrinsic curvature, which may even result in snap-through instability of the equilibrium path as the rotation angle at the entry steadily increases.[2] For this purpose, we apply a partially novel finite element scheme, which is based upon previous works [17,19,20]. We use C^1 continuous cubic finite elements to parametrize both the shape of the deformed shaft axis and the single parameter that governs the rotation of the cross-sections around the axis. While the strain parametrization approach [14] and isogeometric methods [21] are growing in popularity for spatial rod problems, the present approach demonstrates rapid mesh convergence and allows for a very concise implementation, which we provide as supplementary material for the present contribution. The numerical simulations are validated against the analytical solution at small initial curvatures and allow investigating the snap-through instability of the shaft with unconstrained bending deformation. Comparing to the case of the shaft confined in a rigid channel, we observe qualitatively similar behavior, but the effect of initial curvature is more pronounced in the unconstrained case, especially at high values of the angular length of the shaft.

2. Problem statement

In Fig. 1 we plot a flexible shaft confined in a rigid housing without friction such that the cross-sections of the shaft may not move in the transverse direction, but their rotation about the axis is free from kinematic constraints.

Both the shaft in its undeformed state and the channel have the form of a plane circular arc; however, the curvature radii of the two may differ. The length of the shaft is ℓ, and its cross-sections are symmetric such that the bending stiffness is the same in all directions. We parametrize the axis of the shaft by the material coordinate s, which is the arc coordinate in the undeformed state and is counted from the entry point. At the entry point, the rotation angle θ_{entry} is initiated by the driving motor. The shaft is inextensible, which means that s remains the arc coordinate also during the deformation. Because of the initial curvature and torsional flexibility, the rotation will be unevenly distributed in the shaft even in the absence of torque loading at the exit, and the rotation angle becomes a function of the coordinate:

$$\theta = \theta(s), \quad \theta(0) = \theta_{\text{entry}}, \quad \theta(\ell) = \theta_{\text{exit}}. \tag{1}$$

The reason for this is clear: configurations where the directions of the curvatures of the channel and the shaft coincide are energetically more favorable than those with opposite directions of the curvatures, because in the latter case the shaft needs to be bent more strongly to fit into the channel. Thus, changing θ_{entry}, we first increase the elastic energy of the system, which is then released after the peak. It is also understandable that, under certain circumstances, the shaft may slip out of the channel during rotation. An example of the reverse situation can be seen in the benchmark problem of a rigid sleeve sliding along a helicoidal beam, as presented in [22]. In general, the axial motion of the rod within a channel is a result of configurational forces acting at the ends of the rod due to a mismatch between the natural curvatures of the rod and the channel, see [23,24]. To avoid this effect, we hold the axial position of the entry point of the shaft. Along with the inextensibility constraint, this prevents the spatial positions of the cross-sections from changing, allowing only for a change in the rotation angle θ. While the general differential equation for $\theta(s)$ for arbitrary curved and twisted shapes of the rigid channel and the undeformed shaft is derived in [2,16], we restrict our consideration to the simple case of planar circular arcs. We denote the curvature radius of the channel by R, whereas for the shaft it is more convenient to define its curvature κ, which vanishes for an ideally straight line. The respective boundary value problem and its solutions are briefly discussed in Section 3 below.

The novel problem formulation with the freely deformable axis of the shaft is shown in Fig. 2. Both the entry and the end points are clamped so that the rotation about the axial direction is possible, but there are no further kinematic constraints. The locations and the directions of the clamping conditions match those of the constrained case: in the absence of initial curvature, $\kappa = 0$ and the shaft would bend into a circular arc of length ℓ with the curvature radius R, depicted by the dashed line.

3. Analytical solution for the flexible shaft in a rigid channel

The relations of the theory of Kirchhoff rods, presented in Appendix, quickly provide us with the equation for the rotation angle

[2] Some researchers use the term *snap-through instability* when the loading parameter is a force and prefer to speak about *snap-back instability* in case of kinematic loading as in the problem at hand, see, e.g., [7]. Nevertheless, this is not a general convention. For instance, in [6] the authors make no distinction between the types of the loading and write, "Snap-through occurs when a system is in an equilibrium state that either ceases to exist or becomes unstable as a control parameter varies: the system must jump to another equilibrium state". Interestingly, the cited paper deals with branching of elastic equilibria of thin rods under kinematic loading.

$\theta(s)$, because the geometry of the axis of the shaft remains unchanged in the constrained case. We introduce a cylindrical coordinate system with basis vectors

$$\boldsymbol{k}, \quad \boldsymbol{e}_r(\varphi) = -\partial_\varphi \boldsymbol{e}_\varphi, \quad \boldsymbol{e}_\varphi(\varphi) = \partial_\varphi \boldsymbol{e}_r. \tag{2}$$

Here, $\varphi = s/R$ is the angle and $\boldsymbol{r} = R\boldsymbol{e}_r$ is the position vector of the particle of the rod, see Fig. 3; the notation ∂_φ is used for the partial derivative with respect to φ. The local basis vectors, which rotate with the particle, result in

$$\boldsymbol{e}_1 = \boldsymbol{k}\cos\theta + \boldsymbol{e}_r \sin\theta, \quad \boldsymbol{e}_2 = -\boldsymbol{k}\sin\theta + \boldsymbol{e}_r\cos\theta, \quad \boldsymbol{e}_3 = \boldsymbol{r}' = \boldsymbol{e}_\varphi; \tag{3}$$

the rod is inextensible, and the prime denotes the derivative with respect to the material coordinate: $(\cdots)' = \partial_s(\cdots)$. According to the law of summation of angular velocities (in which now the material coordinate s plays the role of time), we obtain the vector of twist and curvature

$$\boldsymbol{\Omega} = \boldsymbol{D} + \theta' \boldsymbol{e}_\varphi \tag{4}$$

with the Darboux vector of the circular arc

$$\boldsymbol{D} = R^{-1}\boldsymbol{k}. \tag{5}$$

Finding the curvatures and twist Ω_i as scalar products Eq. (A.4), we obtain the components of the vector of moments Eq. (A.5) to

$$M_1 = a(R^{-1}\cos\theta - \kappa), \quad M_2 = -aR^{-1}\sin\theta, \quad M_3 = a_t\theta'. \tag{6}$$

The initial curvature κ lies in the plane of the channel when $\theta = 0$ and is thus directed along $\boldsymbol{e}_1$: $\mathring{\Omega}_1 = \kappa$, $\mathring{\Omega}_2 = \mathring{\Omega}_3 = 0$. To obtain the single differential equation for θ, we project the equation of balance of moments Eq. (A.2) onto the tangential direction $\boldsymbol{e}_\varphi$. As

$$\boldsymbol{e}_\varphi \cdot \boldsymbol{r}' \times \boldsymbol{Q} = \boldsymbol{Q}\cdot \boldsymbol{e}_\varphi \times R\boldsymbol{e}_r' = 0 \tag{7}$$

(see Eqs. (2), (3) and the text in between), we find

$$\boldsymbol{e}_\varphi \cdot \boldsymbol{M}' = M_1 \boldsymbol{e}_\varphi \cdot \boldsymbol{e}_1' + M_2 \boldsymbol{e}_\varphi \cdot \boldsymbol{e}_2' + M_3' = 0 \tag{8}$$

because $\boldsymbol{e}_\varphi \boldsymbol{e}_1 = \boldsymbol{e}_\varphi \boldsymbol{e}_2 = \boldsymbol{e}_\varphi \boldsymbol{e}_3' = 0$. Differentiating the same orthogonality conditions with respect to s, we obtain $\boldsymbol{e}_\varphi \cdot \boldsymbol{e}_{1,2}' = -\boldsymbol{e}_{1,2}\cdot \boldsymbol{e}_\varphi'$ with

$$\boldsymbol{e}_\varphi' = \partial_\varphi \boldsymbol{e}_\varphi \, \varphi' = -R^{-1}\boldsymbol{e}_r, \tag{9}$$

such that the balance of twisting moment Eq. (8) now reads

$$M_3' + R^{-1}\boldsymbol{e}_r \cdot (M_1\boldsymbol{e}_1 + M_2\boldsymbol{e}_2) = M_3' + R^{-1}(M_1\sin\theta + M_2\cos\theta) = 0. \tag{10}$$

By substituting Eq. (6) and simplifying, we arrive at the desired differential equation

$$a_t\theta'' - aR^{-1}\kappa\sin\theta = 0. \tag{11}$$

Along with the kinematic boundary condition at the driving end and the vanishing torque loading condition at the driven end, $M_3|_{s=\ell} = 0$, this equation provides the simple looking boundary value problem with a parameter p:

$$\theta'' = p^2\sin\theta, \quad \theta(0) = \theta_{\text{entry}}, \quad \theta'(\ell) = 0, \quad p^2 = \frac{\kappa}{R}\frac{a}{a_t}. \tag{12}$$

Clearly, $\theta = \theta_{\text{exit}} = \theta_{\text{entry}}$ holds in the absence of initial curvature $\kappa = 0$, and the response $\theta_{\text{exit}}(\theta_{\text{entry}})$ becomes identical. When $p^2 > 0$, two additional trivial solutions, where $\theta_{\text{entry}} = 0$ and $\theta_{\text{entry}} = \pi$, are possible, causing the right-hand side of the differential equation to become zero. While the general solution of the boundary value problem can be written in terms of elliptic functions as in [7,8], it is nowadays easier to use numerical integration and the shooting method to fulfill the boundary conditions. The response function $\theta_{\text{exit}}(\theta_{\text{entry}})$ is plotted in Fig. 4 for different values of the dimensionless parameter combination $p\ell$. Technically, the plots were obtained by varying $\theta(\ell) = \theta_{\text{exit}}$ from 0 to 2π and integrating an initial value problem from $s = \ell$ to $s = 0$, which provided the value θ_{entry} necessary for plotting.

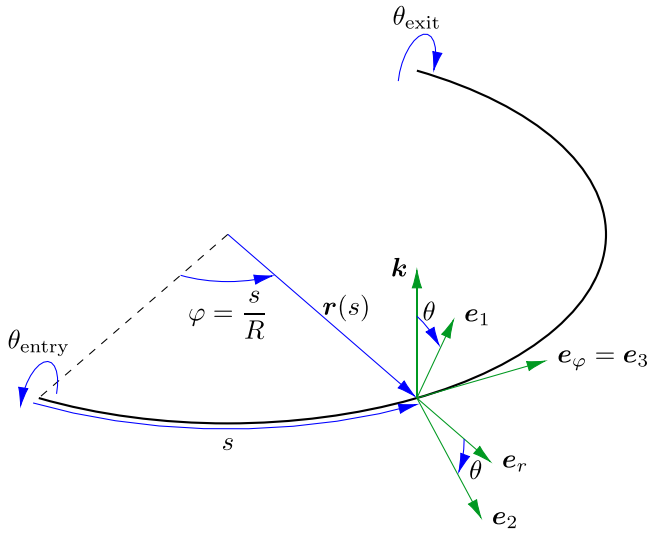

Fig. 3. Geometry of the constrained shaft; the local basis $\boldsymbol{e}_1$, $\boldsymbol{e}_2$, $\boldsymbol{e}_3$ is rotated by angle θ relative to the basis of the cylindrical coordinate system $\boldsymbol{k}$, $\boldsymbol{e}_r$, $\boldsymbol{e}_\varphi$ around the tangential direction $\boldsymbol{e}_\varphi$.

Analyzing the plots, we see that the mapping $\theta_{\text{exit}}(\theta_{\text{entry}})$ is single valued at $p\ell = \pi/4$ and $p\ell = \pi/2$, although a vertical asymptote is visible at $\theta_{\text{entry}} = \theta_{\text{exit}} = \pi$ in the latter case, i.e., when the curvatures of the shaft and channel are directed opposite to each other. As the initial curvature grows further and $p\ell > \pi/2$, multiple equilibria become possible for at least some of the values of θ_{entry}: three at $p\ell = \pi$ and even five at $p\ell = 2\pi$. The pitchfork bifurcation of the equilibrium path for $\theta_{\text{entry}} = \pi$ when the curvature grows beyond the critical value corresponding to $p\ell = \pi/2$ is easy to demonstrate considering the linearized boundary value problem Eq. (12) for a small increment of the solution δ:

$$\theta = \pi + \delta, \quad \delta'' = p^2\sin(\pi+\delta) \approx -p^2\delta, \quad \delta = A\cos ps + B\sin ps,$$
$$\delta(0) = 0 \quad \Rightarrow \quad A = 0, \quad \delta'(\ell) = 0 \quad \Rightarrow \quad \cos p\ell = 0. \tag{13}$$

The smallest eigenvalue is the critical parameter combination, which means existence of adjacent equilibria and thus the onset of instability of the conservative system at hand. In accordance with this conclusion, the equilibrium path for $p\ell = \pi$ contains two stable branches and an unstable one, in which the response θ_{exit} is falling at growing θ_{entry}. Rotating the driving end uniformly, one would observe much slower growth of the angle at the exit until $\theta_{\text{entry}} \approx 4.65$, when the snap-through instability causes the system to jump to the upper part of the equilibrium path after a dynamic process. Further analysis will be necessary to answer the question whether the solution $\theta_{\text{entry}} = \theta_{\text{exit}} = \theta = \pi$ is stable at even higher values of p: among five possible equilibria at $\theta_{\text{entry}} = \pi$ and $p = 2\pi$ (which corresponds to close values of the curvatures of the channel and shaft), three are located on growing parts of the response function, which, however, does not guarantee stability of the system with distributed parameters at hand.

4. Freely deformable flexible shaft: perturbation analysis when the initial curvature is small

The deformability of the axis of the rod makes the goal of finding general analytical solutions of the nonlinear differential equations of Appendix practically hopeless, because $\boldsymbol{r}'$ is unknown in the equation of balance of moments. Nevertheless, it is still possible to obtain the response function in a closed form if one assumes the initial curvature to be small. The unperturbed solution follows at $\kappa = 0$. The shape of the axis of the rod is determined by the channel, there is no torsion, the

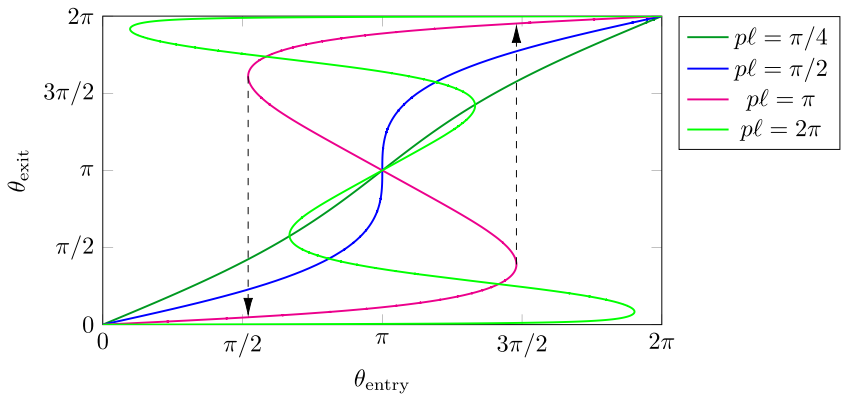

Fig. 4. Elastic response of the curved flexible shaft $\theta_{\text{exit}}(\theta_{\text{entry}})$ for various values of the dimensionless parameter combination $p\ell$; dashed lines depict snap-through and snap-back.

constant bending moment has just the out-of-plane component owing to the isotropy of the cross-section, and the shear force vanishes:

$$\boldsymbol{r} = R\boldsymbol{e}_r, \quad \boldsymbol{Q} = 0, \quad \boldsymbol{M} = aR^{-1}\boldsymbol{k}. \tag{14}$$

Now, we introduce an infinitesimally small initial curvature $\kappa^\bullet$ and are interested in the leading order terms of the changes of the solution variables. The incremental form of Eqs. (A.7) needs to be adjusted, as now not the external loading, but rather the curvature plays the role of the perturbation parameter; see [18] for the application of this technique to another problem formulation.

In the unperturbed state, the rotation of all cross-sections is the same: $\theta = \theta_{\text{entry}}$. There are two thinkable options to take this rotation into account. The first one would be to use the rotated vectors Eq. (3) as the local basis associated with a particle and to let $\kappa^\bullet$ serve as the initial curvature about the first local axis $\mathring{\Omega}_1$, as in the analytical solution for the constrained case. Mathematical transformations are, however, easier if we choose the second option, make use of the symmetry of the cross-section and keep the local basis identical to the basis of the cylindrical coordinate system: $\{\boldsymbol{e}_1, \boldsymbol{e}_2, \boldsymbol{e}_3\} = \{\boldsymbol{k}, \boldsymbol{e}_r, \boldsymbol{e}_\varphi\}$. The preliminary uniform rotation determines the curvature components of the undeformed configuration:

$$\mathring{\Omega}_1 = \kappa^\bullet \cos\theta_{\text{entry}}, \quad \mathring{\Omega}_2 = \kappa^\bullet \sin\theta_{\text{entry}}, \quad \mathring{\Omega}_3 = 0. \tag{15}$$

Now, we rewrite the incremental constitutive relation Eq. $(A.7)_3$ taking into account the contribution of the increments in the initial curvature Eq. (15) to the bending strain:

$$\boldsymbol{M}^\bullet = \boldsymbol{\vartheta} \times \boldsymbol{M} + \mathbf{a}\cdot(\boldsymbol{\vartheta}' - \kappa^\bullet(\boldsymbol{k}\cos\theta_{\text{entry}} + \boldsymbol{e}_r \sin\theta_{\text{entry}})). \tag{16}$$

We aim at deriving the equations for the components of the unknown vector of small rotation

$$\boldsymbol{\vartheta} = \vartheta_r \boldsymbol{e}_r + \vartheta_\varphi \boldsymbol{e}_\varphi + \vartheta_z \boldsymbol{k}. \tag{17}$$

The tensor of bending and torsional stiffness retains its look regardless of the rotation about the axial direction,

$$\mathbf{a} = a(\boldsymbol{k}\boldsymbol{k} + \boldsymbol{e}_r\boldsymbol{e}_r) + a_t \boldsymbol{e}_\varphi \boldsymbol{e}_\varphi, \tag{18}$$

the derivatives of the basis vectors with respect to s are written as in Eqs. (2), (9), and the increment in the vector of moments results in

$$\boldsymbol{M}^\bullet = a(\vartheta_r' - \kappa^\bullet \sin\theta_{\text{entry}})\boldsymbol{e}_r + (a_t\vartheta_\varphi' - R^{-1}(a-a_t)\vartheta_r)\boldsymbol{e}_\varphi + a(\vartheta_z' - \kappa^\bullet\cos\theta_{\text{entry}})\boldsymbol{k}. \tag{19}$$

No distributed forces act on the shaft, $\boldsymbol{q}^\bullet = 0$, which means $\boldsymbol{Q}^\bullet = \text{const}$, and the last term in the linearized equation of moments Eq. $(A.7)_2$ evaluates into

$$\boldsymbol{r}' \times \boldsymbol{Q}^\bullet = \boldsymbol{e}_\varphi \times \boldsymbol{Q}^\bullet = Q_z^\bullet \boldsymbol{e}_r + \cdots \boldsymbol{k}, \tag{20}$$

in which the symbol $\cdots$ comprises the components of $\boldsymbol{Q}^\bullet$ in the plane $\boldsymbol{e}_r$, $\boldsymbol{e}_\varphi$ that are not relevant for the subsequent analysis.

By computing the derivative of Eq. (19) with respect to s, taking into account $\boldsymbol{Q} = 0$ and using Eq. (20), we write the equation of balance of moments Eq. $(A.7)_2$. We further multiply this equation by R and project it onto $\boldsymbol{e}_r$ and $\boldsymbol{e}_\varphi$, which provides us with differential equations for the components ϑ_r and ϑ_φ:

$$\begin{aligned} &aR\vartheta_r'' - a_t\vartheta_\varphi' + (a-a_t)R^{-1}\vartheta_r + Q_z^\bullet R = 0, \\ &a_t R\vartheta_\varphi'' + a_t\vartheta_r' - a\kappa^\bullet \sin\theta_{\text{entry}} = 0. \end{aligned} \tag{21}$$

The projection of balance of moments on $\boldsymbol{k}$ provides a decoupled homogeneous equation for ϑ_z, whose solution is trivial. The solution of the linear system with constant coefficients Eq. (21) features four integration constants, the fifth one is the unknown force component $Q_z^\bullet$. On the other hand, there are three evident kinematic boundary conditions at our disposal: the rotation about the axis is prescribed at the driving end $s = 0$ such that no increment is possible, and the tangential direction may not change at both ends, so that

$$\vartheta_\varphi(0) = 0, \quad \vartheta_r(0) = 0, \quad \vartheta_r(\ell) = 0. \tag{22}$$

The fourth boundary condition expresses the absence of torque loading at the driven end (see Eqs. (19), (22)):

$$M_\varphi^\bullet\big|_{s=\ell} = a_t\vartheta_\varphi'(\ell) - R^{-1}(a-a_t)\vartheta_r(\ell) = 0 \quad \Rightarrow \quad \vartheta_\varphi'(\ell) = 0. \tag{23}$$

To obtain the fifth condition, we need to address the displacements, which follow by integration of Eq. $(A.7)_4$ and must vanish at both ends. Thus, for the vertical displacement component we write

$$u_z' = \boldsymbol{k}\cdot\boldsymbol{\vartheta}\times\boldsymbol{e}_\varphi = \boldsymbol{\vartheta}\cdot\boldsymbol{e}_\varphi \times \boldsymbol{k} = \boldsymbol{\vartheta}\cdot\boldsymbol{e}_r = \vartheta_r, \tag{24}$$

and the necessary condition reads now

$$\int_0^\ell \vartheta_r \,\mathrm{d}s = 0. \tag{25}$$

Upon integrating the second equation in Eq. (21) and using the last boundary condition in Eq. (22) along with the condition Eq. (23), we get the relation between ϑ_r and ϑ_φ':

$$\vartheta_r = -R\vartheta_\varphi' + \frac{a}{a_t}\kappa^\bullet \sin\theta_{\text{entry}}(s-\ell). \tag{26}$$

Using Eqs. (26) and (25), we determine the response function at the exit of the shaft:

$$\begin{aligned} &\int_0^\ell R\vartheta_\varphi' \,\mathrm{d}s = \int_0^\ell \left(\frac{a}{a_t}\kappa^\bullet \sin\theta_{\text{entry}}(s-\ell)\right)\mathrm{d}s \quad \Rightarrow \\ &\Rightarrow \quad \theta_{\text{exit}} - \theta_{\text{entry}} = \vartheta_\varphi(\ell) = -\kappa^\bullet \frac{a\ell^2}{2a_t R}\sin\theta_{\text{entry}}. \end{aligned} \tag{27}$$

To determine the entire deformation in the interior of the domain, we substitute Eq. (26) into the first equation in Eq. (21) and solve the resulting differential equation of third order with integration constants

$C_{1,2,3}$:

$$\vartheta_\varphi = C_1 \cos\frac{s}{R} + C_2 \sin\frac{s}{R} + \frac{a-a_t}{2a_tR}\kappa^\bullet \sin\theta_{\text{entry}}\, s^2 - \\ - \left(\frac{a-a_t}{a_tR}\kappa^\bullet \sin\theta_{\text{entry}}\,\ell - \frac{Q_z^\bullet R}{a}\right) s - \frac{a-a_t}{a_t} R\kappa^\bullet \sin\theta_{\text{entry}} - C_3. \tag{28}$$

Eq. (26) and the second condition in Eq. (22) provide us with a further boundary condition for ϑ_φ:

$$\vartheta'_\varphi(0) = -\frac{a}{a_tR}\kappa^\bullet \sin\theta_{\text{entry}}\ell. \tag{29}$$

The boundary conditions $(22)_1$, (23), (27) and (29) are used to determine the remaining four unknowns $Q_z^\bullet$, $C_{1,2,3}$. The final solution to the boundary value problem reads

$$\vartheta_\varphi = -\frac{\kappa^\bullet \sin\theta_{\text{entry}}}{2R}\left(\left(2\frac{a}{a_t}-1\right)\ell s - \left(\frac{a}{a_t}-1\right)s^2 + \right. \\ \left. + \ell R\left(\sin\frac{s}{R} - 2\cot\frac{\ell}{2R}\sin^2\frac{s}{2R}\right)\right). \tag{30}$$

Let us compare this result to the case of the shaft confined in a channel. For small angles of rotation

$$\theta - \theta_{\text{entry}} \ll 1. \tag{31}$$

This simplifies the boundary value problem Eq. (12):

$$\theta'' = p^2 \sin\theta \approx p^2 \sin\theta_{\text{entry}} \\ \theta(0) = \theta_{\text{entry}}, \quad \theta'(\ell) = 0. \tag{32}$$

Although the linearized solution

$$\theta \approx \theta_{\text{entry}} - \kappa^\bullet \frac{a(2\ell - s)s}{2a_tR}\sin\theta_{\text{entry}} \tag{33}$$

is different from the above one Eq. (30) in the interior domain, the response at the exit is identical to Eq. (27):

$$\theta_{\text{exit}} - \theta_{\text{entry}} \approx -\kappa^\bullet \frac{a\ell^2}{2a_tR}\sin\theta_{\text{entry}}. \tag{34}$$

5. Finite element scheme for large deformations of freely deformable shaft

The observation that both the constrained and free shafts exhibit the same elastic response in the linear range prompts the question of whether this behavior persists for moderately large initial curvatures. In the following, we solve the nonlinear problem numerically using a simple finite element scheme for spatial deformations of Kirchhoff rods, similar to the one previously presented in [17,19,20,25]. Discretizing the deformed configuration of the rod's axis $\boldsymbol{r}(s)$ to fulfill the C^1 interelement continuity conditions is straightforward with the following approximation on an element:

$$\boldsymbol{r} = \boldsymbol{r}_i S_1(\xi) + \partial_\xi \boldsymbol{r}_i S_2(\xi) + \boldsymbol{r}_j S_3(\xi) + \partial_\xi \boldsymbol{r}_j S_4(\xi). \tag{35}$$

The local coordinate ξ on the element is equal to -1 at node i and 1 at node j, which bound the element with the domain $-1 \le \xi \le 1$. The mapping to the material coordinate is linear as long as all elements are equally long:

$$s = \frac{1}{2}\ell_{\text{fe}}\xi + s_0, \quad \ell_{\text{fe}} = \frac{\ell}{n}, \quad \boldsymbol{r}' = \frac{2\,\partial_\xi \boldsymbol{r}}{\ell_{\text{fe}}} \tag{36}$$

where ℓ_{fe} is the material length of each element, n is the number of elements in the model and s_0 determines the coordinate of the middle point of a specific element. Using the position vector $\boldsymbol{r}_i$ and its derivatives $\partial_\xi \boldsymbol{r}_i$ as nodal degrees of freedom guarantees the necessary smoothness of the approximation: both $\boldsymbol{r}(s)$ and $\boldsymbol{r}'(s)$ remain continuous between the elements. The shape functions, which are cubic polynomials in ξ, are uniquely defined by the conditions

$$S_i(-1) = \delta_{i1}, \quad \partial_\xi S_i(-1) = \delta_{i2}, \quad S_i(1) = \delta_{i3}, \quad \partial_\xi S_i(1) = \delta_{i4} \tag{37}$$

with $\delta_{ij} = 1$ if $i = j$ and 0 otherwise being Kronecker's delta; see [26] for more details regarding this approximation with classical Hermite shape functions. Importantly, the inextensibility constraint cannot be exactly fulfilled; therefore, we take into account a small axial strain

$$\varepsilon = \frac{1}{2}(\boldsymbol{r}'\cdot\boldsymbol{r}' - 1) \approx |\boldsymbol{r}'| - 1. \tag{38}$$

The important question of parametrizing the rotation of particles of the rod [27,28] needs to be answered accounting for the no shear constraint of the Kirchhoff theory. Just a single rotation parameter $\psi(s)$ shall smoothly describe the rotation of the basis vectors so that $\boldsymbol{e}_3$ remains tangential to the axis of the beam:

$$\boldsymbol{e}_3 = \frac{\boldsymbol{r}'}{|\boldsymbol{r}'|}. \tag{39}$$

For the specific problem at hand, we use a reference direction $\hat{\boldsymbol{e}} = \boldsymbol{k}$ for that purpose and introduce an intermediate local basis

$$\tilde{\boldsymbol{e}}_3 = \boldsymbol{e}_3, \quad \tilde{\boldsymbol{e}}_1 = \frac{\hat{\boldsymbol{e}} - \hat{\boldsymbol{e}}\cdot\boldsymbol{e}_3\boldsymbol{e}_3}{|\hat{\boldsymbol{e}} - \hat{\boldsymbol{e}}\cdot\boldsymbol{e}_3\boldsymbol{e}_3|}, \quad \tilde{\boldsymbol{e}}_2 = \tilde{\boldsymbol{e}}_3 \times \boldsymbol{e}_1, \tag{40}$$

in which $\tilde{\boldsymbol{e}}_1$ is the projection of the reference direction onto the plane of the cross-section. The intermediate basis is then rotated by the angle ψ to construct the actual deformed one:

$$\boldsymbol{e}_1 = \tilde{\boldsymbol{e}}_1 \cos\psi + \tilde{\boldsymbol{e}}_2 \sin\psi, \\ \boldsymbol{e}_2 = -\tilde{\boldsymbol{e}}_1 \sin\psi + \tilde{\boldsymbol{e}}_2 \cos\psi. \tag{41}$$

As long as the axis of the rod $\boldsymbol{r}'$ does not get parallel to the reference direction $\hat{\boldsymbol{e}} = \boldsymbol{k}$ (which may only happen at very large deformations), no singularity appears in the simulations. In general, updating the director $\hat{\boldsymbol{e}}$ locally at each integration point during time integration helps to address the singularity issue when describing rotations, see this technique in [17]. Although the fixed choice of the reference direction $\hat{\boldsymbol{e}}$ violates the principle of material objectivity and rotating the problem setting in space will result in slightly different specific solutions, this is not a significant concern, because the converged solutions possess this important property, as demonstrated and discussed in Fig. 5.

The functions $\boldsymbol{r}(s)$ and $\psi(s)$ (four scalar variables) fully determine the configuration of the rod and thus the potential energy of the system. The simulations below make use of the cubic C^1 continuous finite element approximation of the rotation parameter

$$\psi = \psi_i S_1(\xi) + \partial_\xi\psi_i S_2(\xi) + \psi_j S_3(\xi) + \partial_\xi\psi_j S_4(\xi), \tag{42}$$

which provides a higher mesh convergence rate in comparison to the linear approximation of ψ used previously in [17,20]. The reason for this is that the curvature and geometric nonlinearity cause bending deformations to also depend on $\psi(s)$ (as shown in Eq. (45) below). Therefore, the high degree of approximation of $\boldsymbol{r}(s)$ becomes efficient for the rate of convergence only together with the respective high-order approximation of the rotation parameter: both approximations are cubic. Each of the $n+1$ nodes of the mesh comprises eight degrees of freedom: three components of $\boldsymbol{r}_i$, three components of $\partial_\xi\boldsymbol{r}_i$, ψ_i and $\partial_\xi\psi_i$.

The implementation of the finite element scheme is concise within the Wolfram Mathematica environment[3] and is provided as supplementary material.[4] The computer algebra helps obtaining the components of the vector of twist and curvature

$$\boldsymbol{\Omega} = \frac{1}{2}\boldsymbol{e}_i \times \boldsymbol{e}_i' = \Omega_i \boldsymbol{e}_i, \quad \Omega_i = \boldsymbol{\Omega}\cdot\boldsymbol{e}_i, \tag{43}$$

in which the law of summation of angular velocities allows first computing the components in regard to the intermediate basis Eq. (40),

$$\tilde{\Omega}_1 = \frac{x'y'' - y'x''}{\sqrt{x'^2+y'^2}\sqrt{x'^2+y'^2+z'^2}}, \\ \tilde{\Omega}_2 = \frac{x'^2z'' + y'^2z'' - x'z'x'' - y'z'y''}{\sqrt{x'^2+y'^2}(x'^2+y'^2+z'^2)}, \\ \tilde{\Omega}_3 = \frac{z'(x'y'' - y'x'')}{(x'^2+y'^2)\sqrt{x'^2+y'^2+z'^2}} \tag{44}$$

[3] https://www.wolfram.com/mathematica/

[4] https://doi.org/10.1016/j.ijnonlinmec.2023.104431

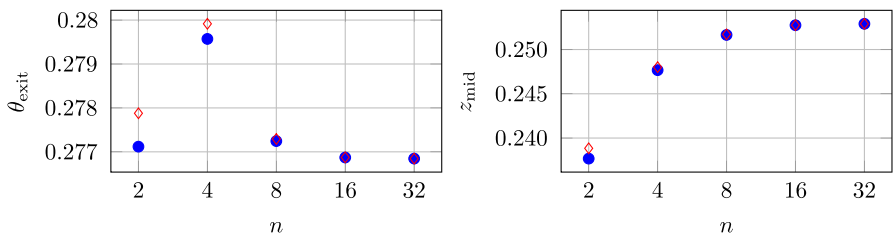

Fig. 5. Mesh convergence study: (*left*) rotation angle at the exit and (*right*) vertical deflection of the middle point at increasing number of finite elements n; filled circles feature reference direction $\hat{\boldsymbol{e}} = \boldsymbol{k}$, while diamond marks correspond to $\hat{\boldsymbol{e}} = \boldsymbol{e}_r$ and justify the objectivity of the converged solution.

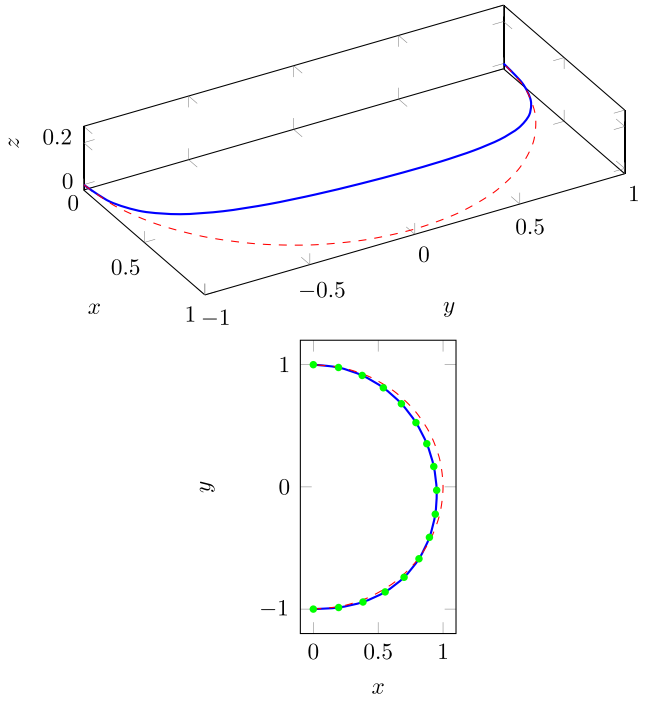

Fig. 6. Deformed shape of the shaft for a high value of initial curvature Eq. (49), isometric projection and top view; dashed red line depicts the ideal undeformed shape, green marks correspond to the nodes of the mesh.

with x, y and z being the Cartesian components of $\boldsymbol{r}$, and then finding the actual curvatures and twist according to

$$\begin{aligned} \Omega_1 &= \tilde{\Omega}_1 \cos\psi + \tilde{\Omega}_2 \sin\psi, \\ \Omega_2 &= -\tilde{\Omega}_1 \sin\psi + \tilde{\Omega}_2 \cos\psi, \\ \Omega_3 &= \tilde{\Omega}_3 + \psi'. \end{aligned} \tag{45}$$

Finally, we minimize the total strain energy with respect to the nodal degrees of freedom:

$$U = \int_0^\ell \frac{1}{2}\left(a(\Omega_1 - \kappa)^2 + a\Omega_2^2 + a_t\Omega_3^2 + b\epsilon^2\right) \mathrm{d}s \to \min. \tag{46}$$

The integration over each finite element is performed using three Gaussian integration points. The kinematic constraints need to be taken into account: $\psi = \theta_{\text{entry}}$ in the very first node, and position vectors as well as the tangential directions $\boldsymbol{e}_3$ are prescribed at both ends of the shaft. We use Wolfram Mathematica to determine the equilibrium by solving the minimization problem presented in Eq. (46) and delegate the computation of the first and second derivatives of U with respect to the degrees of freedom and their subsequent usage in the Newton method to the computer algebra software. The configuration

$$x = R\cos(s/R - \pi/2), \quad y = R\sin(s/R - \pi/2), \quad z = 0, \quad \psi = 0 \tag{47}$$

is used as an initial approximation, unless a specific equilibrium path is sought to be followed as in Fig. 9.

6. Results of finite element analysis: validation and comparison

We used the following standard parameter set for our simulations (presented in SI units throughout this work):

$$\begin{aligned} &R = 1, \quad \ell = \pi R, \quad r = 5\cdot 10^{-3}, \quad E = 2\cdot 10^{11}, \quad \nu = 0.3, \\ &a = E\frac{\pi}{4}r^4, \quad a_t = \frac{E}{2(1+\nu)}\frac{\pi}{2}r^4, \quad b = E\pi r^2. \end{aligned} \tag{48}$$

Here, r is the radius of the circular steel cross-section and the ratio ℓ/R corresponds to a half-circular shape of the shaft in the absence of intrinsic curvature; we will discuss the consequences of increasing the angular length later in this section. The high tension stiffness b allows ignoring the longitudinal extension when comparing to the analytical results.

At first, we investigate the mesh convergence of the finite element model. The chosen high value of the intrinsic curvature enforces large deformations of the shaft with pronounced geometrically nonlinear effects:

$$\kappa = 1, \quad \theta_{\text{entry}} = \pi/2. \tag{49}$$

Beginning with $n = 2$ finite elements, we doubled the detail level of the mesh and repeated the computations, each time collecting the rotation at the exit θ_{exit} and the vertical deflection of the middle node $z_{\text{mid}} = z_{n/2}$, see Fig. 5 for the results. To investigate the material objectivity of the numerical scheme, we also provide the computation results obtained with the reference direction $\hat{\boldsymbol{e}} = \boldsymbol{e}_r$ (thus being the function of s) used for the axial rotation in Eq. (40). The expressions for the twist and curvature components in Eq. (44) become more complicated, and the initial state Eq. (47) now corresponds to $\boldsymbol{e}_1 = \boldsymbol{e}_r$, $\boldsymbol{e}_2 = \boldsymbol{k}$ and $\boldsymbol{e}_3 = \boldsymbol{e}_\varphi$. The intrinsic curvature needs to be added to Ω_2 in the strain energy expression Eq. (46). Although the results are slightly different when the mesh is coarse, the objectivity of the formulation is clearly seen for converged results. At $n = 32$ finite elements, the results with both reference directions become indistinguishable up to 6 decimal places.

We observe that even the coarsest mesh with $n = 2$ finite elements produces quite accurate results. The relative difference between the solutions with 16 and 32 finite elements is below 0.1% for deflections and below 0.01% for the angle of rotation. In the following, we will present the results computed with $n = 16$ finite elements. The deformed shape of the shaft is depicted in Fig. 6. Peculiarly, the vertical deflections are all positive, although the initial curvature of the rod should be directed downwards if $\boldsymbol{e}_1 = \boldsymbol{e}_r$ after rotation by $\theta = \pi/2$.

Comparing the response $\theta_{\text{exit}} \approx 0.277$ (see Fig. 5) with the angle at the entry Eq. (49), we see the difference of $\theta_{\text{exit}} - \theta_{\text{entry}} \approx -1.293$. The analytic expression Eq. (27) for the present parameter set evaluates to the value of -6.415, clearly indicating the inapplicability of the linearized formula for the high value of κ that is considered. The results of finite element computations for values of κ, increasing from zero to some moderate level, are shown in Fig. 7. Preserving $\theta_{\text{entry}} = \pi/2$, we see θ_{exit} first decreasing linearly in accordance to the analytical result Eq. (27), until the nonlinearity starts playing a visible role at $\kappa > 0.1$. Interestingly, the numerical results resemble a saturation curve with a limiting value of θ_{exit}, which can be confirmed by further increasing κ. In Fig. 8 we study the distribution of the rotation angle along the shaft

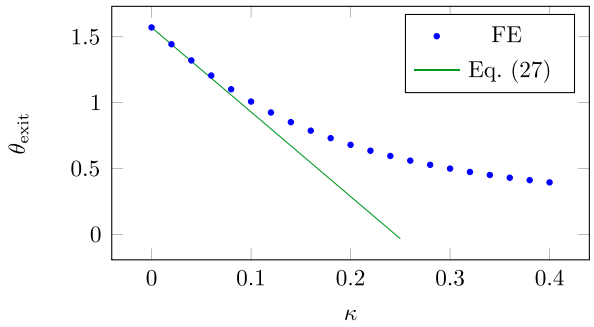

Fig. 7. Elastic response at small κ: exit rotation for $\theta_{\text{entry}} = \pi/2$ at increasing κ, finite element solution (FE) against linearized analytic expression Eq. (27).

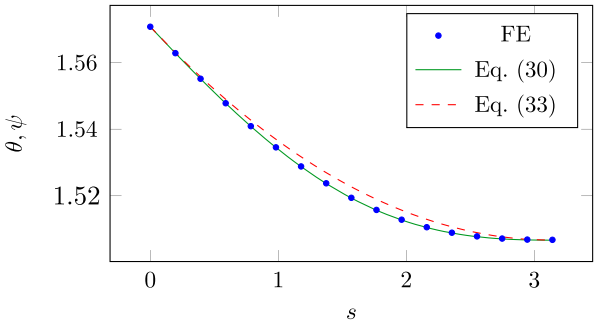

Fig. 8. Elastic response at small κ: distribution of the rotation angle along the shaft at $\kappa = 0.01$, $\theta_{\text{entry}} = \pi/2$, finite element solution (nodal values of ψ), linearized analytic expression Eq. (30) and linearized solution for the constrained case Eq. (33).

$\theta(s)$ for a fixed value $\kappa = 0.1$. The nodal values ψ_i are compared both to $\theta_{\text{entry}} + \vartheta_3$ using the analytical expression Eq. (30) as well as to the simple solution for the constrained case Eq. (33). The numerical and analytical results match perfectly, while the solution for the constrained case indeed produces the same values at the boundaries with a slightly different distribution inside the domain.

Having established the consistence of the numerical model, we use it to evaluate the response $\theta_{\text{exit}}(\theta_{\text{entry}})$ of the freely deformable shaft and to compare it to the case of a shaft in a rigid channel as in Fig. 4. The critical value of the initial curvature for the latter case κ_* follows from

$$p\ell = \sqrt{\frac{\kappa_* a}{Ra_t}}\ell = \frac{\pi}{2} \quad \Rightarrow \quad \kappa_* = \frac{\pi^2 Ra_t}{4\ell^2 a} = \frac{1}{4R(1+\nu)} = 0.1923, \tag{50}$$

where the standard parameter set Eq. (48) was used. In Fig. 9 we plot the response functions for the critical value of the initial curvature, for the twice higher one and for the four times higher one, the last being only ca. 20% below R^{-1}. The equilibrium paths were followed by sweeping θ_{entry} from 0 to 2π and back at small increments, using the solution from the previous step as an initial approximation for the subsequent one. Certainly, only the stable branches could be obtained by minimizing the potential of the system. The dashed lines in the plot correspond to the response of the constrained shaft with the same initial curvature, containing both stable and unstable equilibria. As expected from the analytical results of the linearized problem, we see little difference at smaller values of κ. At $\kappa = 4\kappa_*$, however, the exit rotation angle of the freely deformable shaft may become twice smaller than that of the constrained one. The critical values of θ^*_{entry}, at which the equilibrium becomes unstable and the system snaps through into a non-adjacent configuration, also become different. Interestingly, the snap-through behavior is still associated with a vertical asymptote of the equilibrium path, and we had to use very fine discretization of the load factor θ_{entry} in the vicinity of the critical values θ^*_{entry} to prevent the numerical solver from jumping into a distant equilibrium too early.

From the practical perspective the knowledge of the variation of the critical angle θ^*_{entry} in dependence on the curvature κ may become important. Repeating the simulation for the present parameter set, we collected the data and present an interpolation in Fig. 10 in comparison to the solution for the constrained shaft. The effect of the deformability of the axis of the shaft is getting more pronounced at growing κ. The discontinuity in the plot implies that the scenario of the snap-through behavior changes qualitatively when the initial curvature exceeds the threshold $\kappa_{**} \approx 0.847$: more than a full revolution at the entry is necessary to produce significant rotation at the exit at higher values of κ.

We investigate the effect by plotting the elastic response $\theta_{\text{exit}}(\theta_{\text{entry}})$ until corresponding θ^*_{entry} for values of the initial curvature slightly higher and below κ_{**} in Fig. 11. At $\kappa > \kappa_{**}$, the elastic response is strongly non-monotonous, and the shaft even rotates in the opposite direction at growing θ_{entry} before it finally snaps and makes a full revolution. The 3D configuration of the axis of the shaft for $\kappa = 0.88$ and $\theta_{\text{entry}} = 0.63$ is depicted in Fig. 12. Small increments in θ_{entry} are needed to reach this configuration with a complicated shape of the strongly twisted rod, which is ready to release the accumulated elastic energy and rotate into an almost plane configuration.

Finally, we present the simulation results for the shaft with a higher angular length and consider three fourth of full circle with $\ell = 3\pi R/2$ instead of the standard value Eq. (48). Using the same value of the initial curvature and the entry rotation angle as in Eq. (49), we obtain essentially higher deformations, see Fig. 13. This increased deformability is also apparent in the response function, which is plotted again for three different initial curvature values in Fig. 14. The new critical value of the initial curvature $\kappa_* = 0.08547$ becomes smaller than that in Eq. (50). The response functions of the freely deformable and constrained shafts are significantly different at $\kappa = 4\kappa_*$, and even in the critical case $\kappa = \kappa_*$ the freely deformable shaft demonstrates visible snap-through behavior.

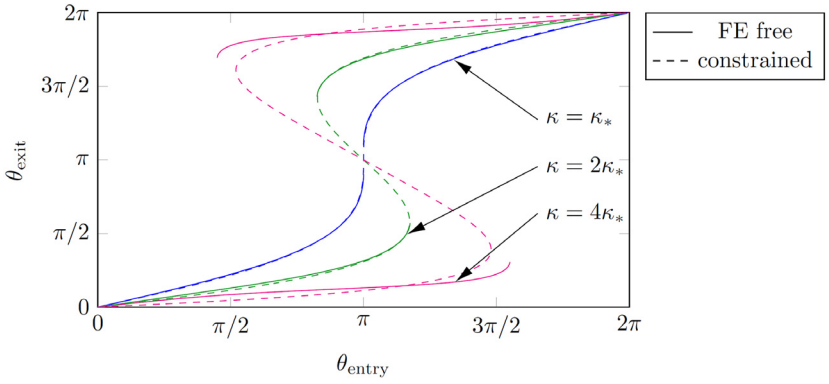

Fig. 9. Response functions for a half-circular flexible shaft at three levels of initial curvature: finite element solutions for a freely deformable shaft vs. semi-analytical results for the shaft confined in a rigid channel.

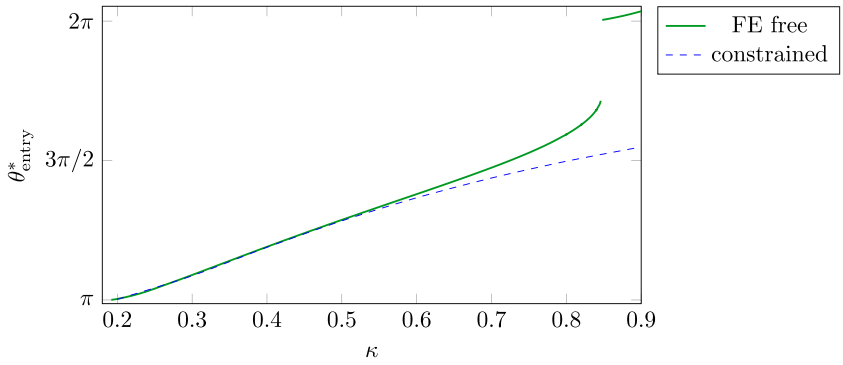

Fig. 10. Variation of the critical entry angle for growing initial curvature, finite element simulations with freely deformable axis vs. semi-analytical results for the shaft constrained in a channel.

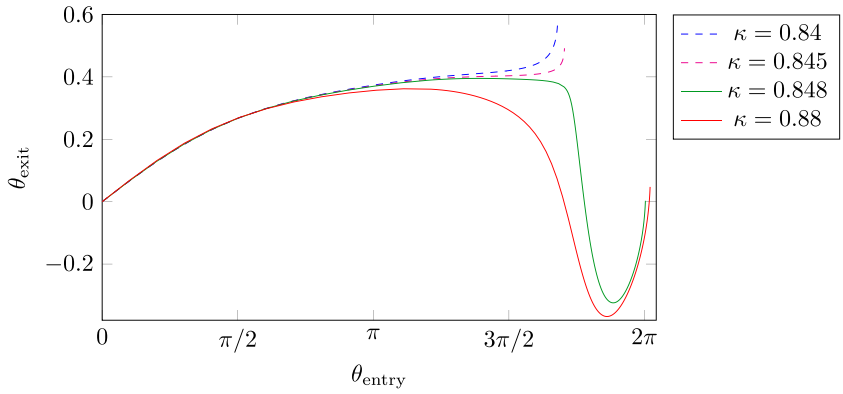

Fig. 11. Lower branches of the response function of a half-circular flexible shaft for values of the initial curvature near the threshold level κ_{**}; snap through happens at more than a full revolution when $\kappa > \kappa_{**}$.

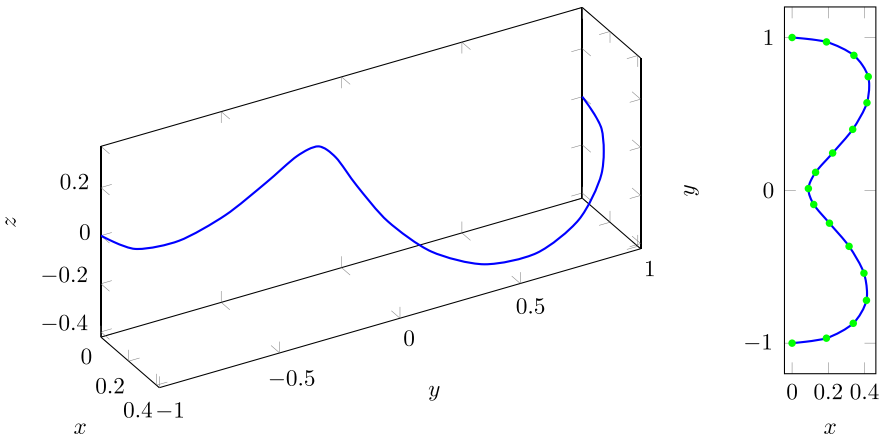

Fig. 12. Deformed shape of the shaft for $\kappa = 0.88$ and $\theta_{\text{entry}} = 6.3$ shortly before the snap-through, isometric projection and top view; see supplementary material for the extended illustration with the orientations of the local basis vectors depicted for better understanding.

7. Conclusions

Both semi-analytical and numerical solutions were developed for the novel problem of transmission of rotary motion by a pre-curved flexible shaft with freely deformable axis. The closed-form solution was obtained by means of the incremental equations of the theory of rods and matches the finite element results when the initial curvature of the shaft is sufficiently small. The simplicity and rapid convergence of the finite element model with C^1 continuous approximation of the position vector and the single rotation parameter allow for an efficient and concise implementation in the framework of Wolfram Mathematica, which is provided as a supplementary material for the present paper. The comparison to previously known solutions for a shaft confined in a rigid channel demonstrates the effect of deformability of the shaft's axis on the response function, namely, the relation between the rotation angles at the driving and the driven ends. Thus, the elastic response function of a shaft with high initial curvature may become essentially non-monotonous with reverse rotation of the driven end while the rotation angle at the entry is steadily increasing. After more than a full revolution of the driving end, a strongly twisted and largely bent rod finally snaps into a nearly flat configuration after a highly dynamical process with a lot of elastic energy released.

We expect that the above presented analytical approach as well as the finite element scheme shall become efficient for modeling the

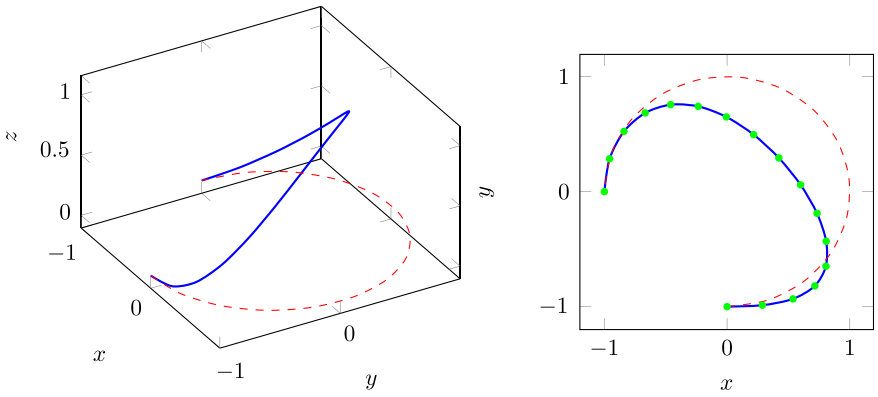

Fig. 13. Deformed shape of the shaft with higher angular length with parameters according to Eq. (49), isometric projection and top view; dashed red line depicts the ideal undeformed shape, green marks correspond to the nodes of the mesh.

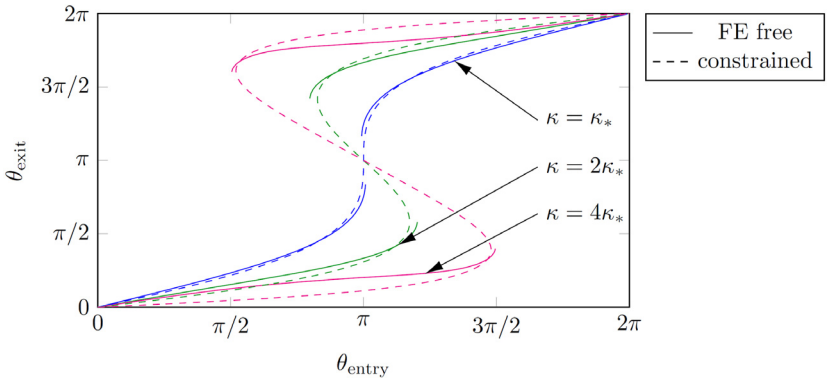

Fig. 14. Response functions for the flexible shaft in the form of three-fourth of a full circle at three levels of initial curvature: finite element solutions for freely deformable shaft vs. semi-analytical results for the shaft confined in a rigid channel.

highly nonlinear spatial behavior of concentric tube robots with initial curvature of both the inner and the outer tubes. A further challenging extension of the presented research is the study of the effect of the unsymmetry of the cross-section in the spirit of [9], whose authors present the results of numerical simulations, but do not reveal the details of the numerical scheme. The rich variety of bifurcations of equilibria of a thin elastic ribbon with rotating ends and the possible influence of the tension on the torsional stiffness of a strip-like cross-section [29] may require validation by means of the shell model as in [18,30].

CRediT authorship contribution statement

Yury Vetyukov: Conceptualization, Methodology, Software, Validation, Formal analysis, Investigation, Data curation, Writing – original draft, Writing – review & editing, Visualization, Project administration. **Evgenii Oborin:** Validation, Formal analysis, Writing – original draft, Writing – review & editing.

Declaration of competing interest

The authors declare that they have no known competing financial interests or personal relationships that could have appeared to influence the work reported in this paper.

Data availability

Simulation code in Wolfram Mathematica is made available online as supplementary material.

Acknowledgments

The authors acknowledge TU Wien Bibliothek, Austria for financial support through its Open Access Funding Programme.

Appendix. Basic relations of the nonlinear theory of Kirchhoff rods and incremental formulation

This is a shortened presentation of the theory in the form derived by Eliseev in [16]; see also [17] for the complete presentation in English.

For a rod being a material line consisting of particles with translational and rotational degrees of freedom, we have the following types of internal force factors: forces and moments. The balance of forces is usually written as

$$\boldsymbol{Q}' + \boldsymbol{q} = 0, \tag{A.1}$$

with $\boldsymbol{q}$ being the vector of external loading per unit length and $\boldsymbol{Q}$ being the internal force vector. Prime denotes the differentiation with respect to material coordinate s, which is chosen to be the arc coordinate of the rod axis in the undeformed configuration. For the purposes of this paper, we ignore external distributed moment loading and write the balance of moments as

$$\boldsymbol{M}' + \boldsymbol{r}' \times \boldsymbol{Q} = 0; \tag{A.2}$$

here, $\boldsymbol{M}$ is the moment vector and $\boldsymbol{r}$ is the position vector of the particle.

To describe the rotation of the rod, we introduce the local basis $\boldsymbol{e}_1$, $\boldsymbol{e}_2$, $\boldsymbol{e}_3$ associated with each particle; the vectors $\boldsymbol{e}_1$ and $\boldsymbol{e}_2$ span the plane of the cross-section and $\boldsymbol{e}_3$ is in the tangential direction to the axis; in our inextensible case, $\boldsymbol{e}_3 = \boldsymbol{r}'(s)$.

The vector of twist and curvature determines the rates of change of the basis vectors along the rod. When s is considered as time, it serves as the angular velocity vector:

$$\boldsymbol{e}_i' = \boldsymbol{\Omega} \times \boldsymbol{e}_i, \quad i = 1 \dots 3. \tag{A.3}$$

The components of the vector of twist and curvature in the local basis

$$\Omega_i = \boldsymbol{e}_i \cdot \boldsymbol{\Omega} \tag{A.4}$$

determine the elastic response in the form of bending and twisting moment

$$\boldsymbol{M} = M_1 \boldsymbol{e}_1 + M_2 \boldsymbol{e}_2 + M_3 \boldsymbol{e}_3 \tag{A.5}$$

with $M_1 = a(\Omega_1 - \mathring{\Omega}_1)$, $M_2 = a(\Omega_2 - \mathring{\Omega}_2)$ and $M_3 = a_t(\Omega_3 - \mathring{\Omega}_3)$. Here, we assume the cross-section to be symmetric with equal bending stiffnesses a in all directions and torsional stiffness a_t. The curvature and twist of the undeformed natural configuration of the rod are determined by the values $\mathring{\Omega}_i$ so that the differences $\Omega_i - \mathring{\Omega}_i$ are the strain measures.

Incremental formulation of the theory of rods is useful if one is interested in the response of the elastic rod to a small perturbation of the model parameters, the boundary conditions or the external loading. The pre-deformed and pre-loaded state of the rod is characterized by the functions $\boldsymbol{r}(s)$, $\boldsymbol{e}_i(s)$, $\boldsymbol{Q}(s)$, $\boldsymbol{M}(s)$, which fulfill the equations of the nonlinear theory with certain distributed external force $\boldsymbol{q}$ and boundary conditions. Focusing for concreteness on a change in the external loading, we consider a close equilibrium with the external force $\boldsymbol{q} + \boldsymbol{q}^\bullet$, in which the dot indicates a small increment of the variable, treated according to the rules of variational calculus. The leading order terms of the increments of the solution variables feature the displacement vector $\boldsymbol{u}$ and the vector of small rotation $\boldsymbol{\vartheta}$:

$$\boldsymbol{r}^\bullet = \boldsymbol{u}, \quad \boldsymbol{e}_i^\bullet = \boldsymbol{\vartheta} \times \boldsymbol{e}_i, \quad \boldsymbol{Q}^\bullet, \quad \boldsymbol{M}^\bullet. \tag{A.6}$$

These variables follow from the equations of the general theory, linearized in the vicinity of a pre-deformed and pre-loaded configuration:

$$\begin{aligned} &\boldsymbol{Q}^\bullet + \boldsymbol{q}^\bullet = 0, \\ &\boldsymbol{M}^{\bullet\prime} + \boldsymbol{u}' \times \boldsymbol{Q} + \boldsymbol{r}' \times \boldsymbol{Q}^\bullet = 0, \\ &\boldsymbol{M}^\bullet = \boldsymbol{\vartheta} \times \boldsymbol{M} + \mathbf{a} \cdot \boldsymbol{\vartheta}', \\ &\boldsymbol{u}' = \boldsymbol{\vartheta} \times \boldsymbol{r}', \end{aligned} \tag{A.7}$$

in which $\mathbf{a} = a(\boldsymbol{e}_1\boldsymbol{e}_1 + \boldsymbol{e}_2\boldsymbol{e}_2) + a_t\boldsymbol{e}_3\boldsymbol{e}_3$ is the tensor of bending and torsional stiffness in the pre-deformed configuration.

Appendix B. Supplementary data

Supplementary material related to this article can be found online at https://doi.org/10.1016/j.ijnonlinmec.2023.104431.

References

[1] Y. Panovko, I. Gubanova, Stability and Oscillation of Elastic Systems: Modern Concepts, Paradoxes and Errors, in: NASA Technical Translation, National Aeronautics and Space Administration, Washington, D.C., 1973.

[2] A.K. Belyaev, V.V. Eliseev, Flexible rod model for the rotation of a drill string in an arbitrary borehole, Acta Mech. 229 (2) (2018) 841–848, http://dx.doi.org/10.1007/s00707-017-2003-4.

[3] G. Pramhas, A. Belyaev, Instabilität einer rotierenden biegsamen Antriebswelle in einem gekrümmten Kanal, Antriebstechnik 37 (11) (1998) 74–76.

[4] V. Eliseev, T. Zinovieva, On transmission of rotation by a flexible shaft, Theoriya Mekh. Mash. 3 (2) (2005) 67–72 (in Russian).

[5] J. Till, V. Aloi, K.E. Riojas, P.L. Anderson, R.J. Webster III, C. Rucker, A dynamic model for concentric tube robots, IEEE Trans. Robot. Autom. 36 (6) (2020) 1704–1718, http://dx.doi.org/10.1109/TRO.2020.3000290.

[6] M. Gomez, D.E. Moulton, D. Vella, Critical slowing down in purely elastic 'snap-through' instabilities, Nat. Phys. 13 (2) (2017) 142–145, http://dx.doi.org/10.1038/nphys3915.

[7] A. Cazzolli, F. Dal Corso, Snapping of elastic strips with controlled ends, Int. J. Solids Struct. 162 (2019) 285–303, http://dx.doi.org/10.1016/j.ijsolstr.2018.12.005.

[8] C. Armanini, F. Dal Corso, D. Misseroni, D. Bigoni, From the elastica compass to the elastica catapult: an essay on the mechanics of soft robot arm, Proc. R. Soc. Lond. Ser. A Math. Phys. Eng. 473 (2198) (2017) 20160870, http://dx.doi.org/10.1098/rspa.2016.0870.

[9] T.G. Sano, H. Wada, Twist-induced snapping in a bent elastic rod and ribbon, Phys. Rev. Lett. 122 (11) (2019) 114301, http://dx.doi.org/10.1103/PhysRevLett.122.114301.

[10] M. Vaz, G. Mascaro, Post-buckling analysis of slender elastic vertical rods subjected to terminal forces and self-weight, Int. J. Non-Linear Mech. 40 (7) (2005) 1049–1056, http://dx.doi.org/10.1016/j.ijnonlinmec.2004.12.002.

[11] R. Singh, J. Tiwari, A. Kumar, Self-contact in closed and open Kirchhoff rods, Int. J. Non-Linear Mech. 137 (2021) 103786, http://dx.doi.org/10.1016/j.ijnonlinmec.2021.103786.

[12] P. Theocaris, D. Panayotounakos, Non-linear elastic analysis of thin rods subjected to bending with arbitrary kinetic conditions of their cross-sections, Int. J. Non-Linear Mech. 17 (2) (1982) 119–128, http://dx.doi.org/10.1016/0020-7462(82)90043-9.

[13] A.A. Sipos, P.L. Várkonyi, The longest soft robotic arm, Int. J. Non-Linear Mech. 119 (2020) 103354, http://dx.doi.org/10.1016/j.ijnonlinmec.2019.103354.

[14] F. Boyer, V. Lebastard, F. Candelier, F. Renda, Dynamics of continuum and soft robots: A strain parameterization based approach, IEEE Trans. Robot. Autom. 37 (3) (2021) 847–863, http://dx.doi.org/10.1109/TRO.2020.3036618.

[15] S. Antman, The theory of rods, in: S. Flügge, C. Truesdell (Eds.), Handbuch der Physik, Vol. VIa/2, Springer, Berlin-Heidelberg-New York, 1972, pp. 641–703.

[16] V. Eliseev, Mechanics of Deformable Solid Bodies (in Russian), St. Petersburg State Polytechnical University Publishing House, St. Petersburg, 2006.

[17] Y. Vetyukov, Nonlinear Mechanics of Thin-WAlled Structures. Asymptotics, Direct Approach and Numerical Analysis, Foundations of Engineering Mechanics, Springer, Vienna, 2014, p. 272, http://dx.doi.org/10.1007/978-3-7091-1777-4.

[18] Y. Vetyukov, C. Schmidrathner, A rod model for large bending and torsion of an elastic strip with a geometrical imperfection, Acta Mech. 230 (11) (2019) 4061–4075, http://dx.doi.org/10.1007/s00707-019-02378-y.

[19] K. Nachbagauer, P.G. Gruber, Y. Vetyukov, J. Gerstmayr, A spatial thin beam finite element based on the absolute nodal coordinate formulation without singularities, in: International Design Engineering Technical Conferences and Computers and Information in Engineering Conference, Vol. 54815, 2011, pp. 909–917, http://dx.doi.org/10.1115/DETC2011-47732.

[20] Y. Vetyukov, V. Eliseev, Modeling of building frames as spatial rod structures with geometric and physical nonlinearities, Vychisl. Mekh. Sploshnykh Sred 3 (3) (2010) 32–45, http://dx.doi.org/10.7242/1999-6691/2010.3.3.25.

[21] E. Marino, J. Kiendl, L. De Lorenzis, Explicit isogeometric collocation for the dynamics of three-dimensional beams undergoing finite motions, Comput. Methods Appl. Mech. Engrg. 343 (2019) 530–549, http://dx.doi.org/10.1016/j.cma.2018.09.005.

[22] S. Han, Configurational forces and geometrically exact formulation of sliding beams in non-material domains, Comput. Methods Appl. Mech. Engrg. 395 (2022) 115063, http://dx.doi.org/10.1016/j.cma.2022.115063.

[23] S. Han, O.A. Bauchau, Configurational forces in variable-length beams for flexible multibody dynamics, Multibody Syst. Dyn. (2022) 1–24, http://dx.doi.org/10.1007/s11044-022-09866-5.

[24] C. Armanini, F. Dal Corso, D. Misseroni, D. Bigoni, Configurational forces and nonlinear structural dynamics, J. Mech. Phys. Solids 130 (2019) 82–100, http://dx.doi.org/10.1016/j.jmps.2019.05.009.

[25] P. Gruber, K. Nachbagauer, Y. Vetyukov, J. Gerstmayr, A novel director-based Bernoulli–Euler beam finite element in absolute nodal coordinate formulation free of geometric singularities, Mech. Sci. 4 (2) (2013) 279–289, http://dx.doi.org/10.5194/ms-4-279-2013.

[26] Y. Vetyukov, Hybrid asymptotic-direct approach to the problem of finite vibrations of a curved layered strip, Acta Mech. 223 (2) (2012) 371–385, http://dx.doi.org/10.1007/s00707-011-0562-3.

[27] S. Florian, C. Damien, Geometrically exact static 3D Cosserat rods problem solved using a shooting method, Int. J. Non-Linear Mech. 119 (2020) 103330, http://dx.doi.org/10.1016/j.ijnonlinmec.2019.103330.

[28] C. Meier, A. Popp, W.A. Wall, Geometrically exact finite element formulations for slender beams: Kirchhoff–Love theory versus Simo–Reissner theory, Arch. Comput. Methods Eng. 26 (1) (2019) 163–243, http://dx.doi.org/10.1007/s11831-017-9232-5.

[29] Y. Vetyukov, Direct approach to elastic deformations and stability of thin-walled rods of open profile, Acta Mech. 200 (3–4) (2008) 167–176, http://dx.doi.org/10.1007/s00707-008-0026-6.

[30] Y. Vetyukov, Stability and supercritical deformation of a circular ring with intrinsic curvature, in: H. Irschik, A. Belyaev, M. Krommer (Eds.), Dynamics and Control of Advanced Structures and Machines, Springer International Publishing, Cham, 2017, pp. 23–32, http://dx.doi.org/10.1007/978-3-319-43080-5_3.